RESEARCH ARTICLE

ADVANCED FUNCTIONAL MATERIALS
www.afm-journal.de

Laser-Induced Graphene-Assisted Patterning and Transfer of Silver Nanowires for Ultra-Conformal Breathable Epidermal Electrodes in Long-Term Electrophysiological Monitoring

Jiuqiang Li, Senhao Zhang, Jun Zhong, Benkun Bao, Kai Guo, Yingying Zhang, Kerong Yang, Yao Tong, Donghai Qiu, Hongbo Yang,* and Huanyu Cheng**

Nanomaterial-based stretchable electronics composed of conductive nanomaterials in elastomer can seamlessly integrate with human skin to imperceptibly capture electrophysiological signals. Despite the use of transfer printing to form embedded structures, it remains challenging to facilely and stably integrate conductive nanomaterials with thin, low-modulus, adhesive elastomers. Here, a facile-yet-simple laser-induced graphene (LIG)-assisted patterning and transfer method is demonstrated to integrate patterned silver nanowires onto an ultra-low modulus silicone adhesive as ultra-conformal epidermal electrodes. The resulting thin epidermal electrodes of ≈50 µm exhibit a low sheet resistance (0.781 Ω sq^{-1}), tissue-like Young's modulus (0.53 MPa), strong self-adhesion, and excellent breathability. The breathable electrodes dynamically conformed to the skin with low contact impedance allow for long-term, high-fidelity monitoring of electrophysiological signals in complex environments (even during exercise and heavy sweating). Moreover, the LIG-assisted transfer can provide a robust interface to establish a stable connection between the soft electrodes and rigid hardware. The large-scale fabrication further provides an eight-channel electromyography system combined with a deep learning algorithm for gesture classification and recognition with remarkable accuracy (95.4%). The results from this study also provide design guidelines and fabrication methods of the next-generation epidermal electronics for long-term dynamic health monitoring, prosthetic control, and human-robot collaborations.

1. Introduction

Epidermal electronics, known for their skin-like properties, refer to electronic devices mounted on the skin with stable physiological signal outputs, which play a vital role in health monitoring, disease diagnosis, and human-machine interfaces.[1] Compared with traditional rigid wearable devices, epidermal electronics with a modulus close to that of skin could deform with skin to maintain good conformal contact during natural motions/deformations, which reduces motion artifacts and allows for continuous, long-term monitoring while minimizing discomfort.[2]

Electrophysiological signals such as electrocardiograms (ECG), electromyograms (EMG), electrooculograms (EOG), electroencephalograms (EEG), etc., generated during human muscular activities, contain a wealth of physiological information that reflects the body's health status.[3] Long-term monitoring of these signals offers a wider temporal perspective, allowing for the acquisition of more comprehensive health information and enhancing the ability to detect transient and subtle anomalies, which can improve the diagnostic accuracy of related diseases (such as epilepsy,[4] atrial fibrillation,[5] and muscle atrophy).[6] The non-invasive monitoring of epidermal electrophysiological signals typically relies on the use of bioelectrodes mounted on the skin surface.[7] The most commonly used Ag/AgCl electrodes for electrophysiological monitoring are associated with limitations such as dehydration, high skin contact impedance, skin inflammation,

---

J. Li, J. Zhong, B. Bao, K. Guo, Y. Zhang, K. Yang, Y. Tong, H. Yang
School of Biomedical Engineering (Suzhou)
Division of Life Sciences and Medicine
University of Science and Technology of China
Hefei 230022, P. R. China
E-mail: yanghb@sibet.ac.cn

The ORCID identification number(s) for the author(s) of this article can be found under https://doi.org/10.1002/adfm.202504481

DOI: 10.1002/adfm.202504481

J. Li, S. Zhang, J. Zhong, B. Bao, K. Guo, Y. Zhang, K. Yang, Y. Tong, D. Qiu, H. Yang
Suzhou Institute of Biomedical Engineering and Technology
Chinese Academy of Science
Suzhou 215011, P. R. China
E-mail: zhangsh@sibet.ac.cn

S. Zhang, H. Cheng
Department of Engineering Science and Mechanics
The Pennsylvania State University
University Park
Pennsylvania 16802, USA
E-mail: huanyu.cheng@psu.edu

S. Zhang
Jinan Guoke Medical Technology Development Co., Ltd
Jinan 250101, P. R. China

and performance degradation from motion artifacts. Therefore, they are unsuitable for accurate electrophysiological monitoring under complex conditions such as long-term monitoring and exercise accompanied by heavy sweating.[8] To obtain high-quality electrophysiological signals with low motion artifacts in these complex situations, dry electrodes with high conformability and breathability, along with low contact impedance, are highly desirable.[9] Good conformality facilitates a seamless skin/electrode interface to establish a stable and unhindered signal pathway, which can be realized by reduced bending stiffness (from decreased thickness and modulus). The stable performance over motions often hinges on strong adhesion at the electrode/skin interface.[10] In addition, inevitable perspiration during long-term monitoring triggers signal distortion due to adhesion failure at the skin/electrode interface, and the residual moisture further causes skin irritation and user compliance issues.[11] Furthermore, a low-impedance skin-electrode interface is also crucial for accurate monitoring of electrophysiological signals, which usually comes from the high conductivity of the electrode.[12] Therefore, it has been the central focus to develop epidermal electrodes with minimized thickness and modulus, enhanced breathability, conductivity, and excellent adhesion (along with easy removal if possible).

Although conductive patterns can be directly formed on the low-modulus elastomer surface with 3D printing or spray coating,[13] they often suffer from weak interfacial adhesion and require complex surface treatments to avoid delamination.[14] The ultra-thin metal film patterned into a mesh layout by photolithography or laser cutting can be subsequently transferred and printed onto thin soft, stretchable substrates,[15] but the interface is still not sufficiently strong and the fabrication also needs to use sophisticated fabrication equipment and complex surface functionalization.[16] In addition, the connection between electrodes and rigid data acquisition systems with commercial conductive pastes (e.g., anisotropic conductive film cables and silver paste) often suffers from interfacial failure upon deformation due to mechanical mismatch.[17] Transfer printing technology often relies on pre-deposition on a donor substrate and subsequent physical transfer,[18] which allows the conductive nanomaterial network to be embedded into the polymer matrix for enhanced mechanical stability.[19] The conductive nanomaterial network with good electrical conductivity and stretchability is crucial for establishing a stable, low-impedance skin/electrode interface.[20] Compared with the other types of conductive nanomaterials such as nanoparticles or nanosheets, nanowires such as AgNWs with large aspect ratios can exhibit high metallic conductivity at low percolation thresholds for improved optical transparency.[21] As a result, the composite features a large surface coverage of the adhesive polymer for enhanced adhesion and facile connection with rigid data acquisition modules in a plug-and-play manner. It is relatively easy to completely transfer the AgNWs network to high-modulus, low-adhesion substrates such as poly(methyl methacrylate), polyimide (PI), polyvinyl alcohol (PVA), and poly(dimethylsiloxane) (PDMS). However, van der Waals forces between the deposited AgNWs network and the donor substrate increase the difficulty of the transfer,[22] where the target ultra-thin, low-modulus soft elastomers often cannot supply sufficient gripping force to overcome the van der Waals forces, causing irreversible damage to the AgNWs network with low transferring yields. Thus, successful complete transfer often requires exploring the target elastomer with high modulus and reduced adhesion, leading to compromised conformality.

Efforts to address this challenge led to 1) chemical modifying the elastomer to facilitate the formation of robust chemical bonding with the AgNWs and 2) tuning the rigidity of the elastomer for improved gripping force during transfer. The former can include Ag-N bonding between AgNWs and bipyridine-modified PDMS or the Triton-X-doped PDMS,[19b,23] but the limited material choices and sophisticated modification methods present challenges for large-scale industrialization. The representative effort in the latter exploits a cryo-transfer technique that freezes PDMS in liquid nitrogen (N_2) with a temporarily increased modulus.[24] As the PDMS returns to its initial low-modulus state when attached to the skin, the epidermal electrode with the entire AgNWs network successfully transferred to the ultra-thin (8.4 μm) PDMS exhibits a sheet resistance of 13.2 Ω sq^{-1} and conforms to the skin for monitoring electrophysiological signals. Similarly, silk fibroin with tunable rigidity through changes in relative humidity can also transfer stretchable metal networks with high yields.[25] However, the complex operation and strict environmental requirements make it difficult to be widely used.

In addition, customized high-density surface electromyography (sEMG) and full-scalp EEG measurements require complex patterning of electrodes over a large scale.[2a,26] Although mask spraying and screen printing can be exploited,[14,27] these two commonly used patterning methods have low material utilization rates and usually require customized masks, which often cannot be reused due to sample/ink residuals after use, leading to significantly increased preparation time and costs. Other patterning techniques such as maskless inkjet printing can directly print AgNWs on target elastomer,[28] but ink composition and rheology need intricate optimization and nozzle clogging also hinders repeated use. Thus, it is essential to develop AgNWs transfer technique that is scalable, universal, easy to pattern, and low-cost yet highly efficient.

This work explores laser-induced graphene (LIG)-assisted transferring and patterning of the AgNWs network onto an ultra-thin, breathable, self-adhesive, low-modulus stretchable substrate to provide epidermal electrodes for ultra-long-term, dynamic monitoring of electrophysiological signals in complex environments (**Figure 1**a). Due to its lower contact angle with solvents and weaker van der Waals forces with the AgNWs network, the patterned porous LIG allows facile transfer of the patterned AgNWs network onto the soft, adhesive stretchable substrate through a simple sticking and peeling-off process with near 100% yield. The resulting electrodes with the patterned AgNWs network on the representative substrate that combines styrene-ethylene-butylene-styrene block copolymer (SEBS) with Silbione of extremely low modulus (7 kPa) and strong adhesion (80 Nm^{-1}) can conform to the skin with low contact impedance and reduced motion artifacts (Figure 1b-i). The entire preparation process is simple yet efficient and suitable for the preparation of large-area epidermal electrode arrays with complex patterns. With periodic perforation provided by the same laser, the porous substrate together with the AgNWs network provides the resulting epidermal electrodes with breathable properties and reduced effective modulus to form excellent dynamic conformal contact with the skin and maintain stable adhesion even during

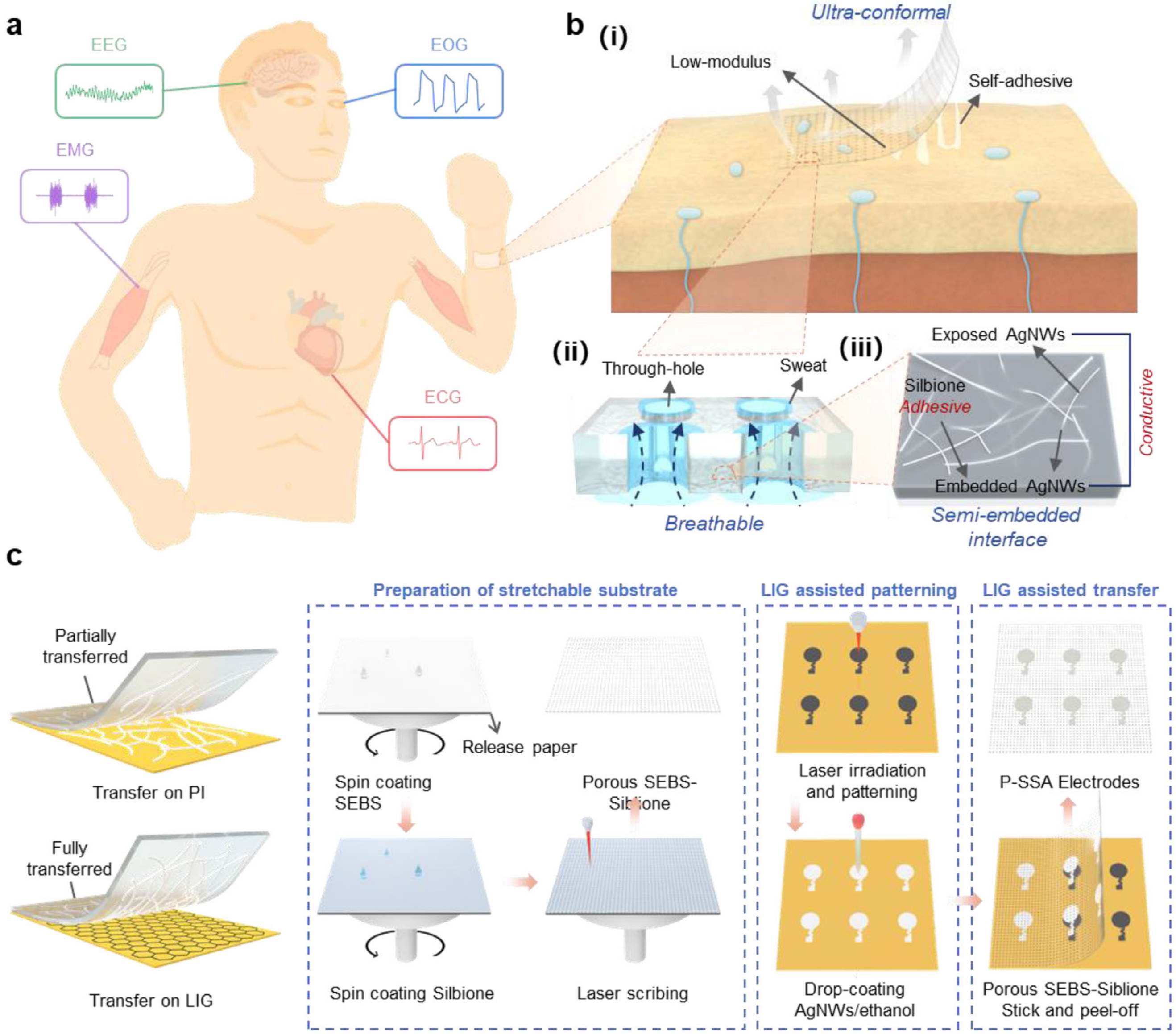

Figure 1. Schematic illustration of the fabrication and application of porous SEBS-Silbione-AgNWs (P-SSA) epidermal electrodes. a) Application of P-SSA electrodes for dynamic monitoring of electrophysiological signals, such as electrocardiograms (ECG), electromyograms (EMG), electrooculograms (EOG), and electroencephalograms (EEG). b) (i) Desirable properties of the epidermal electrodes for long-term monitoring during exercise due to (ii) breathable design and (iii) adhesive surface of the P-SSA electrode. c) Fabrication of the P-SSA epidermal electrodes, with the inset showing the important role of the porous laser-induced graphene (LIG) during the transfer process of the silver nanowires (AgNWs) network.

sweating (Figure 1b-ii). In addition, the adhesive epidermal electrode can facilely establish a stable connection with rigid data acquisition modules by simple pressing without using adhesives/pastes (Figure 1b-iii). As a result, the porous SEBS-Silbione-AgNWs (P-SSA) epidermal electrodes exhibit outstanding long-term, wireless, and dynamic monitoring of high-quality electrophysiological signals in complex real-world scenarios. The P-SSA epidermal electrodes configured into a two by eight array and combined with a deep learning algorithm further result in an 8-channel EMG system for gesture recognition of eight common gestures with an excellent accuracy rate of 95.4%. The design, fabrication, and application of the P-SSA epidermal electrodes pave the way for future imperceptible electronics for high-precision, ultra-long-term monitoring of electrophysiological and other vital signals for early disease diagnostics, timely treatment evaluations, and accurate prosthetic controls.

2. Results and Discussion

2.1. Skin-Conformal Epidermal Electrodes Prepared by LIG-Assisted Transfer Printing

Compared to the other methods that only focus on the changes in the target elastomer, we modulate the donor substrate for simultaneous transfer and patterning with improved efficiency. Inspired by previous studies that explore graphene with a weak van der Waals interface to assist the transfer of metal films,[22] patterned hydrophilic and porous LIG prepared from a single-step laser scribing over a large scale can assist in the almost complete transfer (near 100%) and easy patterning of AgNWs without other environment and equipment requirements. Compared to traditional chemical vapor deposition (CVD) and graphite exfoliation methods used to prepare graphene,[29] the fabrication method from this study also offers the advantages of simplicity, lower cost, and easy-to-pattern. The fabrication starts with i) the preparation of an ultra-thin, breathable, self-adhesive stretchable substrate and ii) simultaneous LIG-assisted patterning of AgNWs network, followed by iii) transfer printing of patterned AgNWs from LIG onto the stretchable substrate via a simple mechanical peeling (Figure 1c).

The stretchable substrate with a bi-layered design consists of an elastomeric SEBS with excellent elasticity on top of a low-modulus Silbione adhesive. The top ultra-thin, non-adhesive SEBS film provides mechanical support for conductive AgNWs while ensuring easy removal from the donor release paper after applying to the skin, whereas the bottom Silbione ensures sufficient adhesion strength to the skin for long-duration wear. The donor release paper serves as a temporary support layer to prevent the electrical failure of the AgNWs-elastomer conductive network during the transfer printing (removed after skin attachment). In addition, micro perforations of circular hole arrays with a diameter of 0.16 mm and a spacing of 0.64 mm in the substrate obtained with the 10.6 µm CO_2 laser enhance the permeability of the air and water molecules. Next, patterned porous LIG prepared on commercial polyimide (PI) films using the same CO_2 laser has more polar bonds (C─O, C═O) and other oxygenated groups,[30] exhibiting a smaller ethanol contact angle compared to PI (Figure S1, Supporting Information). Therefore, the AgNWs dispersion (diameter of 90 nm and length of 60 µm) in ethanol drop-coated onto the LIG pattern would be dispersed uniformly on the entire LIG pattern without flowing onto the PI. As ethanol evaporates, a freestanding AgNWs network with the same pattern as the LIG forms on the surface and can be easily exfoliated mechanically due to the weak van der Waals surface and porous nature of the LIG. Lastly, applying the previously prepared stretchable substrate with the Silbione adhesive facing the AgNWs/LIG surface followed by a gentle pressure embeds the AgNWs network into the top surface of the elastomer. Moreover, the low modulus of the top Silbione and uneven porous surface of LIG is favorable for the semi-embedding of AgNWs during the LIG-assisted transfer, establishing a stable electrical connection to resist delamination failure during motion (Figure S2, Supporting Information). The AgNWs network with a natural porous structure (Figure S3, Supporting Information) combined with the perforated substrate yields ultra-conformal and breathable epidermal electrodes.

2.2. Mechanism of LIG-Assisted Transfer Printing and Patterning of the AgNWs Network

Characterizations of the microstructures of the AgNWs/LIG and AgNWs/PI interfaces help elucidate the mechanism of LIG-assisted transfer. The scanning electron microscope (SEM) image reveals a clear boundary and line contacts between the AgNWs and the LIG (**Figure 2a-i**) due to the van der Waals surface of graphene and thus no interfacial products. Furthermore, the wrinkles and porous structure of the LIG surface further reduce the contact area with the AgNWs and lower the interfacial energy, resulting in a high transfer yield (Figure 2b-i). In contrast, the interface between the PI and the AgNWs exhibits fuzzy boundaries and face contacts (Figure 2a-ii), which probably results from the dispersant (polyvinylpyrrolidone, PVP) of the AgNWs solution deposited at the interface to form a semicircular shape in the cross-sectional view (Figure 2b-ii). Additionally, the smooth surface of the PI provides a larger contact area with the AgNWs to increase the interfacial energy and adhesion, presenting difficulty in transfer.

The easily detachable amorphous carbon on the LIG surface also facilitates the transfer of the AgNWs from LIG to the stretchable SEBS-Silbione substrate (Figure 2c). Compared with no carbon particles on the AgNWs transferred from PI, carbon particles are evident on the surface of the AgNWs transferred from LIG or even the transferred LIG (in the control without AgNWs on LIG) (Figure 2d-i). Raman spectra of the transferred surfaces reveal characteristic D peak (≈1350 cm^{-1}), G peak (≈1580 cm^{-1}), and 2D peak (≈2700 cm^{-1}) for the transferred LIG, along with the increased width of D and G peaks but the absence of the 2D peak to indicate amorphous carbon for the AgNWs transferred from LIG (Figure 2d-ii).[29a] In contrast, the AgNWs transferred from PI do not exhibit any characteristic peaks of graphene or amorphous carbon. In the survey of energy dispersive X-ray spectroscopy (EDS), the transferred LIG surfaces display decreased energy of the C peak and the absence of the Ag peak. Taken together with the presence of Ag and C elements on the transferred SEBS-Silbione elastomer surface (Figure 2e-i), the results indicate that the AgNWs and part of the amorphous carbon have been successfully transferred from the LIG surface to the elastomer surface. Moreover, the elemental mapping images (Figure 2e-ii) clearly show a uniform distribution of the C element on the elastomer surface. Meanwhile, when amorphous carbon is removed from the LIG surface with repeated taping (Figure 2f), the yield of the LIG-assisted transfer calculated by counting the AgNWs on the LIG surface before and after the transfer is sharply decreased from 95.7 ± 1.5% to 23.6 ± 12.7% (Figure 2g; Figures S4 and S5, Supporting Information). Collectively, the above results confirm the critical role of the amorphous carbon on the LIG surface in facilitating the transfer process of AgNWs.

The low interfacial energy between porous LIG and AgNWs, together with the easily detachable amorphous carbon on the LIG surface, can result in a high transfer yield at room temperature for the LIG-assisted transfer. Compared with a partial transfer (also with damage) of the AgNWs deposited on PI, AgNWs deposited on LIG are almost completely damage-free transferred to the soft SEBS-Silbione substrate (Figure S6, Supporting Information), and the yield of the LIG-assisted transfer is significantly higher than 30.8 ± 4.2% (or 16.2 ± 8.1%) for the direct transfer from the PI (or glass) (Figure S7, Supporting Information), which demonstrates the salient advantages of LIG-assisted transfer. The increase in the laser flux varies the surface morphology of the induced graphene: incomplete patterning, laser-induced graphene, laser-induced graphene fibers (LIGF), carbon nanoparticles, and complete ablation (Figure S8, Supporting Information).[31] The

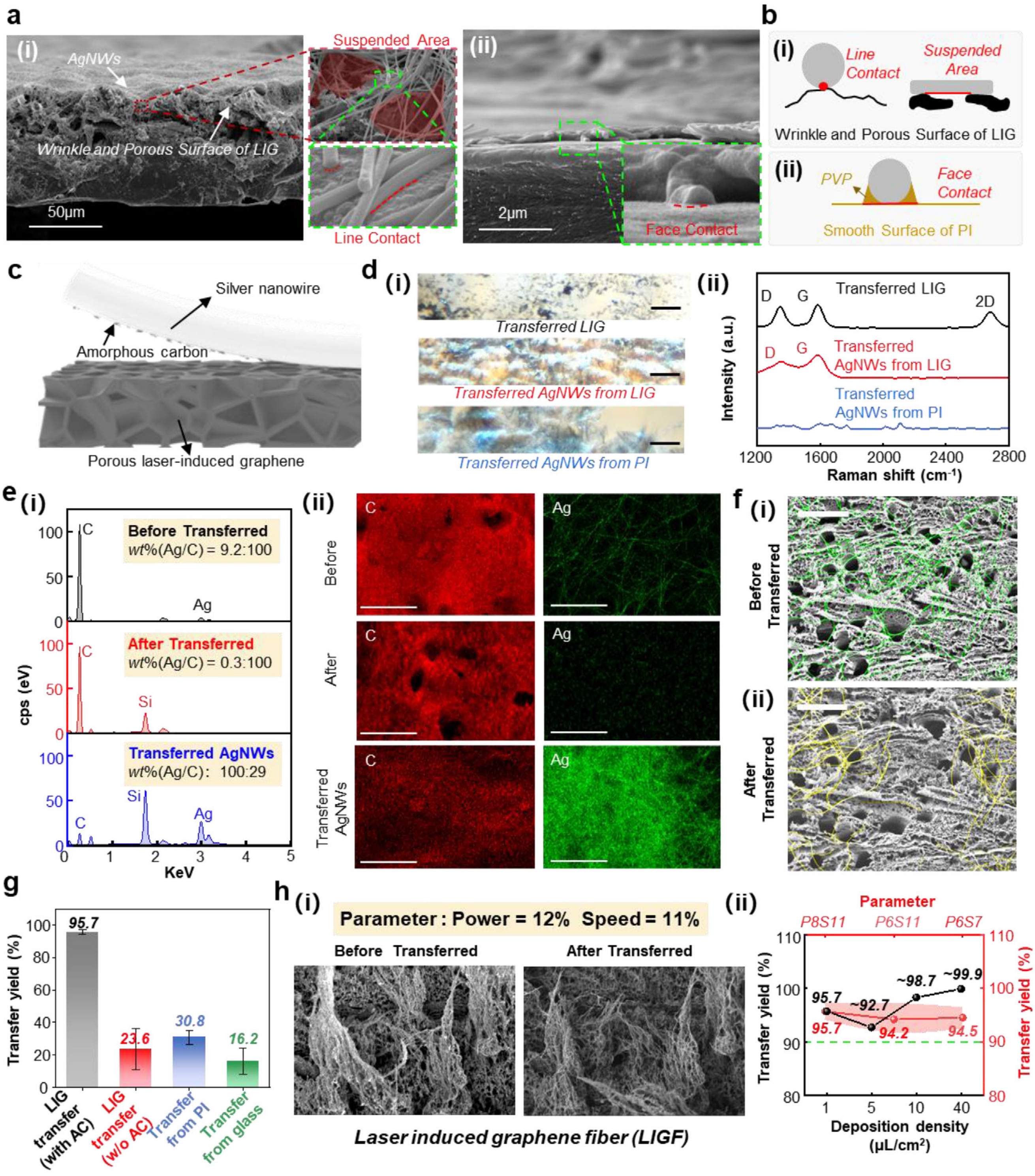

Figure 2. Mechanism and advantages of LIG-assisted transfer. a) Scanning electron microscope (SEM) images of AgNWs deposited on (i) LIG and (ii) polyimide (PI). b) Schematic diagram showing the difference in the contact area between AgNWs and LIG (top) or PI (bottom). c) Schematic diagram showing the critical role of amorphous carbon in LIG-assisted transfer printing. d) (i) Optical microscopy images and (ii) Raman spectra of transferred LIG, AgNWs transferred from LIG, and AgNWs transferred from PI. Scale bar, 50 µm. e) (i) Energy dispersive X-ray spectroscopy (EDS), and (ii) distribution of AgNWs deposited on LIG before (top) and after (middle) transfer, along with Silbione-AgNWs transferred from LIG (bottom). f) (i) SEM images of AgNWs deposited on LIG without amorphous carbon before (top) and after (bottom) transfer. g) Comparison in transfer yield between LIG-assisted transfer (with and without amorphous carbon) and direct transfer from PI and glass (N = 3). h) (i) SEM images of AgNWs deposited on laser-induced graphene fiber (LIGF) before (left) and after (right) transfer. (ii) Transfer yield of LIG-assisted transfer at different laser parameters (P8S11: power = 8%, speed = 11%; P6S11: power = 6%, speed = 11%; P6S7: power = 6%, speed = 7%) as a function of the AgNWs deposition density (N = 3).

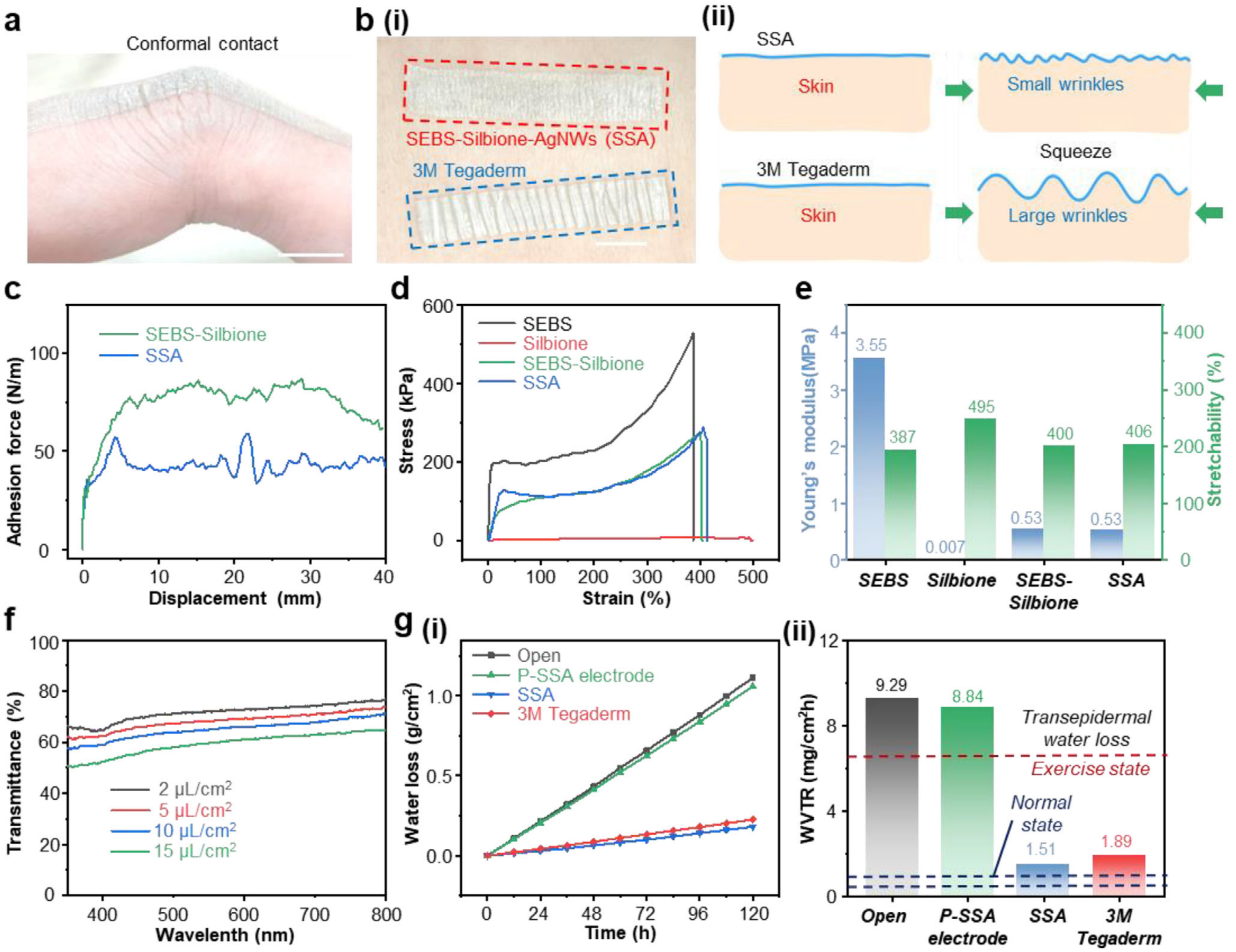

Figure 3. Evaluation of conformality and breathability of P-SSA epidermal electrodes. Photographs of (a) the SEBS-Silbione-AgNWs composite (SSA) attached to the finger joint and (b) (i) the SSA along with 3 M Tegaderm with AgNWs transferred by LIG-assisted transfer printing attached to the forearm. Scale bar, 1 cm. (ii) Schematic illustration of the wrinkle-generating mechanism. c) Adhesion force versus displacement curves of the SEBS-Silbione substrate with and without AgNWs. d) Tensile stress-strain curves of SEBS, Silbione, SEBS-Silbione, and the SSA composite. e) The comparison in Young's modulus and maximum stretchability of SEBS, Silbione, SEBS-Silbione, and SSA composite. f) Optical transmittance of the SSA composite with different AgNWs deposition densities. g) (i) Water loss versus time and corresponding (ii) water vapor permeability for 3 M Tegaderm, SSA composite, and P-SSA composite.

morphology of incomplete patterning, carbon nanoparticles, and complete ablation is accompanied by the loss of porous graphene structure and amorphous carbon to result in obvious residues of AgNWs. Besides, the presence of some AgNWs on the back of LIGF makes it difficult to be in contact with the SEBS-Silbione substrate (Figure S9, Supporting Information) resulting in incomplete transfer (Figure 2h-i). However, the LIG fabricated from various laser parameters features a consistently high transfer yield, which reaches ≈99.9% as the deposition density of AgNWs increases to 40 μL cm^{-2} (Figure 2h-ii), indicating the versatility of the LIG-assisted patterning and transfer method for AgNWs (Figures S10 and S11, Supporting Information).

In addition, the pattern LIG with a smaller ethanol contact angle also facilitates the AgNWs patterning processing without the mask. Furthermore, linear pattern arrays with varying line widths and spacings fabricated from the CO_2 laser demonstrate minimum achievable feature resolution with a line width of 150 μm and a spacing of 100 μm (Figure S12, Supporting Information).

2.3. Mechanical, Electrical, and Breathable Properties of Skin-Conformal Epidermal Electrodes

The conformal contact of the epidermal electrode to the skin without constraining the natural motions is demonstrated by attaching the SSA composite to a finger joint with a tight fit to the wrinkled skin without any visible detachment (**Figure 3**a).[32] The use of a 50 μm-thick stretchable substrate (Figure S13, Supporting Information) with low-modulus and strong adhesion also allows transfer of a “SIBET”-shaped AgNWs network onto the forearm to form intimate contact with the skin and follow the deformations/motions of the skin (e.g., stretching, compression, and twisting) (Video S1, and Figure S14, Supporting Information). Compared with a medical dressing (3M Tegaderm) that generates large wrinkles due to poor conformability and modulus mismatch with the skin, the SSA composite forms intimate contact with the skin (Figure 3b). In addition, there is no skin irritation after continuous wearing of P-SSA electrodes for 7 days due to the high biocompatibility (Figure S15, Supporting Information). In conclusion, the thin, lower-modulus, stretchable P-SSA electrode results in a minimal constraint on skin deformation to provide a more comfortable wearing experience with almost no foreign body sensation.

A strong and stable adhesion at the electrode/skin interface is key to ensure low contact impedance for accurate acquisition of electrophysiological signals, especially under movements and skin motions/deformations. The standard 90-degree peeling test of the epidermal electrode from dry human skin at a speed of 30 mm min^{-1} is carried out to evaluate the adhesion strength. Although the adhesion (40 N/m) of the SSA composite to the skin is only half of that (80 N m^{-1}) of the SEBS-Silbione stretchable substrate (Figure 3c), it is still larger than most previously reported electrodes (Table S1, Supporting Information). Meanwhile, the practical use of the electrode pattern often explores 25% surface coverage over the entire substrate area to result in a higher adhesion of 70 N m^{-1}. Such high adhesion allows the epidermal electrodes to stably adhere to the skin, but there is no residue when removed (Figure S16, Supporting Information) due to the mechanical robustness of the bi-layered design. The stress-strain curve of the SSA composite (Figure 3d) reveals a lower overall modulus (0.53 MPa) (calculated from the linear range up to 5% strain) and higher stretchability (406%) (Figure 3e). Compared to SBES, Silbione, and SEBS-Silbione films, the SSA composite exhibits almost the same mechanical properties as the SEBS-Silbione composite, which shows decreased Young's modulus and increased stretchability over SEBS due to the use of Silbione. The favorable mechanical properties of the SSA composite allow it to maintain stable contact and adhesion to the skin during large deformation without constraining the skin motion.

The low sheet resistance of the electrode and good contact with the skin contribute to the reduced electrode/skin contact impedance for high-performance recording and stimulation.[12,33] The sheet resistance of the AgNWs network in an 8 mm × 8 mm square measured using a four-point probe drops sharply from 70 to 0.781 Ω sq^{-1} as the AgNWs content increases from 2 to 10 µL cm^{-2} (Figure S17, Supporting Information). Meanwhile, the transparency only decreases slightly from 72.10% to 64.95% (Figure 3f). Additionally, the relative resistance change under stretching shows a larger variation for the sample with increased concentration of AgNWs from 4 to 40 µL cm^{-2} (Figure S18, Supporting Information). Considering a larger variation in the relative resistance change is more likely to introduce motion artifacts, the AgNWs content of 10 µL cm^{-2} exhibits a balance performance with high transparency (≈64.95%), low sheet resistance (≈0.781 Ω sq^{-1}), and small relative resistance changes upon stretching. Therefore, the concentration of 10 µL cm^{-2} is chosen in the following investigations unless otherwise specified. As the vapor permeability of wearable electrodes is key to avoiding skin inflammation and adhesion failure during long-term use,[34] the WVTR test is carried out to evaluate the vapor permeability of the electrodes. The P-SSA electrode with microperforation array exhibits WVTR of 8.84 $\text{mg}\cdot\text{cm}^{-2}\cdot\text{h}^{-1}$, which is almost the same as that of the open bottle (9.29 $\text{mg}\cdot\text{cm}^{-2}\cdot\text{h}^{-1}$) at 25 °C and 25% relative humidity and much larger than that of the non-porous SSA electrode (without microperforation) and 3 M Tegaderm (Figure 3g). In addition, the water vapor transmission rate (WVTR) of the P-SSA electrode is higher than the trans-epidermal water loss during varying levels of exercise (≈0.6–6.6 $\text{mg}\cdot\text{cm}^{-2}\cdot\text{h}^{-1}$).[35] As a result, the electrode does not affect sweat evaporation and is suitable for electrophysiological monitoring during exercise accompanied by heavy sweating.

2.4. Application of Skin-Conformal Epidermal P-SSA Electrodes for ECG Monitoring

Two P-SSA working electrodes placed on the inner wrists of the right and left arms, together with another P-SSA ground electrode on the left foot, record ECG signals over time in complex environmental conditions (**Figure** 4a). As the stable and low-impedance skin-electrode interface supports long-term high-quality monitoring of electrophysiological signals,[36] the skin contact impedance of the P-SSA electrode has been investigated under varying intricate conditions (e.g., dry, sweaty, and stretched) (Figure 4b). Compared with the commercial Ag/AgCl gel electrode, the P-SSA electrodes exhibit lower areal contact impedance in both dry and wet conditions, along with less variation during skin deformation such as stretching. The obtained ECG signal with distinct features of P-wave, QRS-complex, and T-wave (Figure S19, Supporting Information) clearly matches that from the commercial gel electrode even under different motions such as finger pressing, finger stretching, and forearm movements (Figure 4c-i). Compared with the commercial gel electrodes, the P-SSA electrodes exhibit more stable ECG signals with a higher signal-to-noise ratio (SNR) (Figure 4c-ii), especially during finger stretching and forearm movements. The improved tolerance to the dynamic interference from the P-SSA electrodes results from its stable conformal contact with the skin. The excellent breathability also allows the use of P-SSA electrodes for long-term continuous monitoring of the ECG signals over 7 days (Figure 4d-i), with distinguishable PQRST waveform and only a slight decrease from 18.38 to 17.43 in SNR (Figure 4d-ii). Moreover, the ECG signals measured by P-SSA electrodes stored for 200 days in the ambient conditions still maintain a high SNR (≈18.38) that is comparable to the freshly prepared (≈18.64), which is attributed to its consistent high adhesive force (≈31 N m^{-1}) and stretchability (≈404%) (Figure S20, Supporting Information) to ensure a stable electrode-skin interface. In addition, the backside of SEBS-Silbione with a high water contact angle of ≈88° also facilitates the use of P-SSA electrodes in water with high SNR (Figure S21 and Video S2, Supporting Information). The above results build a strong foundation for the P-SSA electrode's long-term usage in daily life with complex conditions, but a stable connection with the data acquisition (DAQ) system is still a challenge.

Modulus mismatch between soft P-SSA electrodes and the rigid DAQ hardware is prone to debonding due to the stress concentration. As the LIG-assisted transfer can integrate AgNWs onto different receiving substrates with varying moduli, a

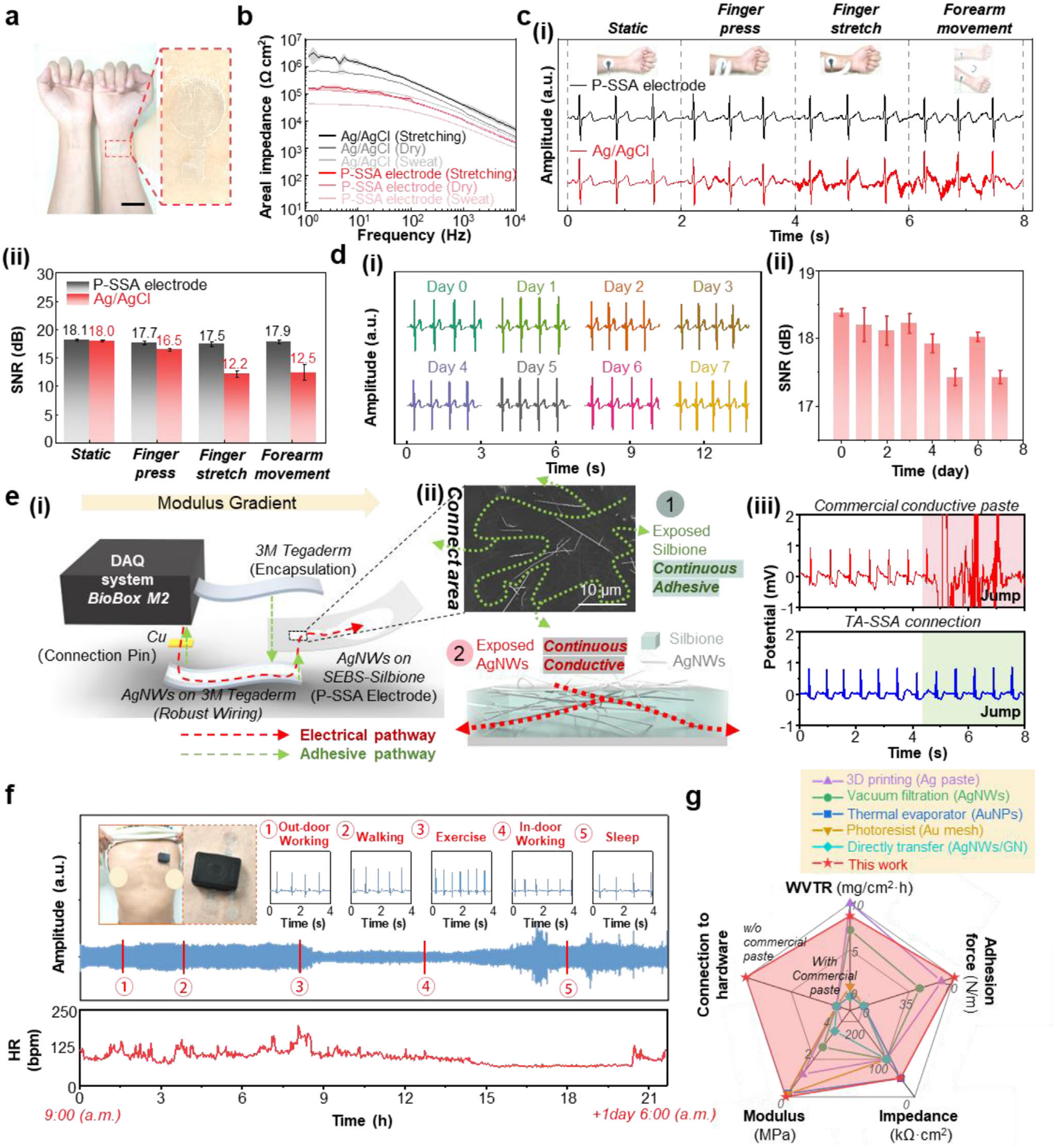

Figure 4. Application of P-SSA epidermal electrodes for high-fidelity long-term, motion artifact-free ECG monitoring. a) Photograph of P-SSA electrodes attached to inner wrists. Scale bar, 5 cm. b) Comparison in the areal skin contact impedance versus frequency between P-SSA electrodes and the commercial Ag/AgCl gel electrodes under dry, sweating, and stretching conditions. c) (i) Comparison in ECG signals measured by P-SSA electrodes and commercial gel electrodes before and after introducing various motion artifacts, along with (ii) the comparison in the corresponding signal-to-noise ratio (SNR). d) (i) Long-term ECG signals measured by P-SSA electrodes at different times and (ii) corresponding SNR. e) (i) Schematic of the connecting interface with gradient modulus design, in which a thick, encapsulated wiring (intermediate modulus) connects the ultrathin, self-adhesive P-SSA electrode (low modulus) with the rigid hardware (high modulus). (ii) Magnified SEM image and illustration of the connecting interface area to show exposed AgNWs and adhesive silicone. (iii) Comparison of the measured ECG signals with traditional paste connection (top) and TAg-SSA connection (bottom) between P-SSA electrodes and hardware. f) Continuous ECG signals wirelessly monitored from the P-SSA electrode on the human subject over 21 h, along with the calculated heart rate. g) Performance comparison between this work and previously reported epidermal electrodes in terms of water vapor transmission rate (WVTR), adhesion force, skin-like modulus, and easiness for hardware integration.

gradient modulus design is facilely achieved by exploiting AgNWs transferred onto 3M Tegaderm (TAg) as a composite with intermediate modulus (≈26.7 MPa) between the P-SSA (≈0.53 MPa) electrode and rigid hardware (Figure 4e-i). The inherently stretchable, adhesive, conductive TAg-SSA interface (Figure S22, Supporting Information) can establish a stable connection between soft P-SSA and rigid Cu pad of the DAQ system in a plug-and-play manner, even upon skin motions and deformations (Figure S23, Supporting Information). The adhesive polymer with a large surface coverage at the pattern area provides high adhesion strength as revealed by the SEM image (Figure 4e-ii), whereas the semi-embedded structure of AgNWs forms the continuous conductive pathway. As a result, the ECG signals collected by the P-SSA electrodes are immune to motion artifacts (Figure 4e-iii). Taken together with the plug-and-play TAg-SSA interface, the ECG signal quality is well maintained during repeated "peeling-and-reattaching" cycles (Figure S24, Supporting Information).

Three P-SSA electrodes self-adhered on the chest and connected to the wireless DAQ system (BioBox M2, Sibet CAS) by the TAg-SSA interface with a gradient modulus allows wireless, continuous long-term ECG recording during varying activities and events in daily life (Video S3, Supporting Information). While a mild baseline shift is observed during high-intensity exercise that generates heavy sweating and skin deformation, the measured raw ECG signals without filtering still exhibit well-preserved characteristic peaks and features, indicating the negligible effect of sweating and motion artifacts on ECG monitoring. Therefore, the integrated sensing system with good breathability, excellent dynamic skin conformality, and stable TAg-SSA interface facilitates wireless, long-term, continuous ECG monitoring over 21 h (Figure 4f). While direct coating of the AgNWs-ethanol solution on the porous SEBS-silicone substrate also prepares the electrode, it is prone to crack formation and unable to record stable ECG signals during skin deformation (Figure S25, Supporting Information). In addition, the directed deposited/coated AgNWs cover a large surface area to reduce adhesion, resulting in electrical failure at the connecting points with the rigid DAQ systems. In comparison, the semi-embedded P-SSA electrodes prepared by the simple-yet-effect LIG-assisted transfer printing provide long-term, high-fidelity monitoring of electrophysiological signals in complex environments (even during exercise and heavy sweating). The comparison of the resulting P-SSA electrodes with other epidermal electrodes fabricated with various methods and materials further highlights the advantages of high WVTR, sufficient yet robust adhesion force, low skin contact impedance, skin-like modulus, and facile hardware integration for long-term monitoring in daily life (Figure 4g, and Table S1, Supporting Information).

2.5. Application of P-SSA Electrodes for EMG, EOG, and EEG Monitoring

Three P-SSA electrodes placed on the wrist flexor muscle (inner forearm) of the human subjects record EMG signals (**Figure** 5a). Grasping elastic balls with increasing gripping strength from 10 to 20 and then to 40 kg leads to increased peak amplitude in the EMG signals, and the larger amplitude recorded by the P-SSA electrodes proves its higher sensitivity than commercial gel electrodes (Figure 5b). The excellent EMG monitoring with the P-SSA electrodes under sweating conditions is highlighted in comparison with commercial gel electrodes (Figure 5c,d). Upon sweating, the SNR of the commercial gel electrodes decreases significantly from 27.8 to 17.5 dB by 37.1%, along with significantly increased baseline noise from 2.1 to 4.8 µV by 128.6%, demonstrating the deteriorating effect of sweat on the EMG monitoring (Figure 5d,e). In contrast, the EMG signals measured by the P-SSA electrode with excellent water vapor permeability only exhibit a slight decrease in the SNR from 33.4 to 29.5 dB by 11.7%, together with a slight increase in the baseline noise from 1.6 to 2.3 µV by 43.8%. As a result, the SSA electrode is more suitable for EMG monitoring in complex scenarios such as sweating, which is confirmed by a 48-h continuous wear experiment (Figure 5f,g). Owing to the excellent conformality and breathability, the P-SSA electrodes exhibit a baseline noise of 1.7 µV, which is lower than that of 2.1 µV from the commercial Ag/AgCl gel electrode (Figure 5h). Different from the commercial electrode with the baseline noise increased significantly from 2.1 to 4.5 µV by 114.3% after 48 h of continuous wear (likely due to the dehydration of the gel), the SSA electrode only features a slight increase in the baseline noise from 1.7 to 2.3 µV by 35.3%. The much smaller drift in the baseline noise (i.e., 33%) from the SSA electrode compared with its commercial gel electrode counterpart over sweating and long-term use highlights its salient performance.

Apart from the significant motion of the muscle fibers from the forearm, low-amplitude EMG signals generated by the finger flexion/extension can also be recorded by the epidermal P-SSA electrodes, which also exhibit higher amplitude than that of Ag/AgCl electrodes (Figure S26, Supporting Information). The enhanced EMG signal quality can contribute to high-precision human-computer interaction.

Placing the P-SSA electrodes near the eye records both vertical EOG and horizontal EOG signals (Figure S27a, Supporting Information). After setting the stable EOG signal when the subject is looking straight ahead as baseline waveform, the deviated waveform from the baseline during eye movements clearly identifies blink signals from the vertical EOG,[37] periodic up/down and side-to-side eye motions (Figure S27b, Supporting Information).

Although EEG signals are of great significance for the diagnosis and therapy of brain diseases, high-quality recording of EEG signals is more challenging than ECG and EMG signals due to the significantly lower magnitude and the presence of the hair.[38] In the proof-of-the-concept demonstration for the EEG monitoring, the test electrode is placed on the forehead (Fp1) with the ground/reference electrodes on the right/left mastoids according to the international 10/20 system (Figure S28a, Supporting Information). The EEG signals in three mental states (i.e., eyes closed, eyes open, and sleeping) (Figure S28b, Supporting Information) with the zoom-in shown in Figure S28c (Supporting Information) display obvious differences in frequency and amplitude. The EEG signals with the eyes closed processed using fast Fourier transform (FFT) exhibit a clear peak ≈9 Hz that is related to the alpha rhythm (Figure S28d, Supporting Information), whereas the EEG signals during eyes open and the sleeping states are mainly concentrated in the low-frequency region (<9 Hz) (Figure S28e,f,

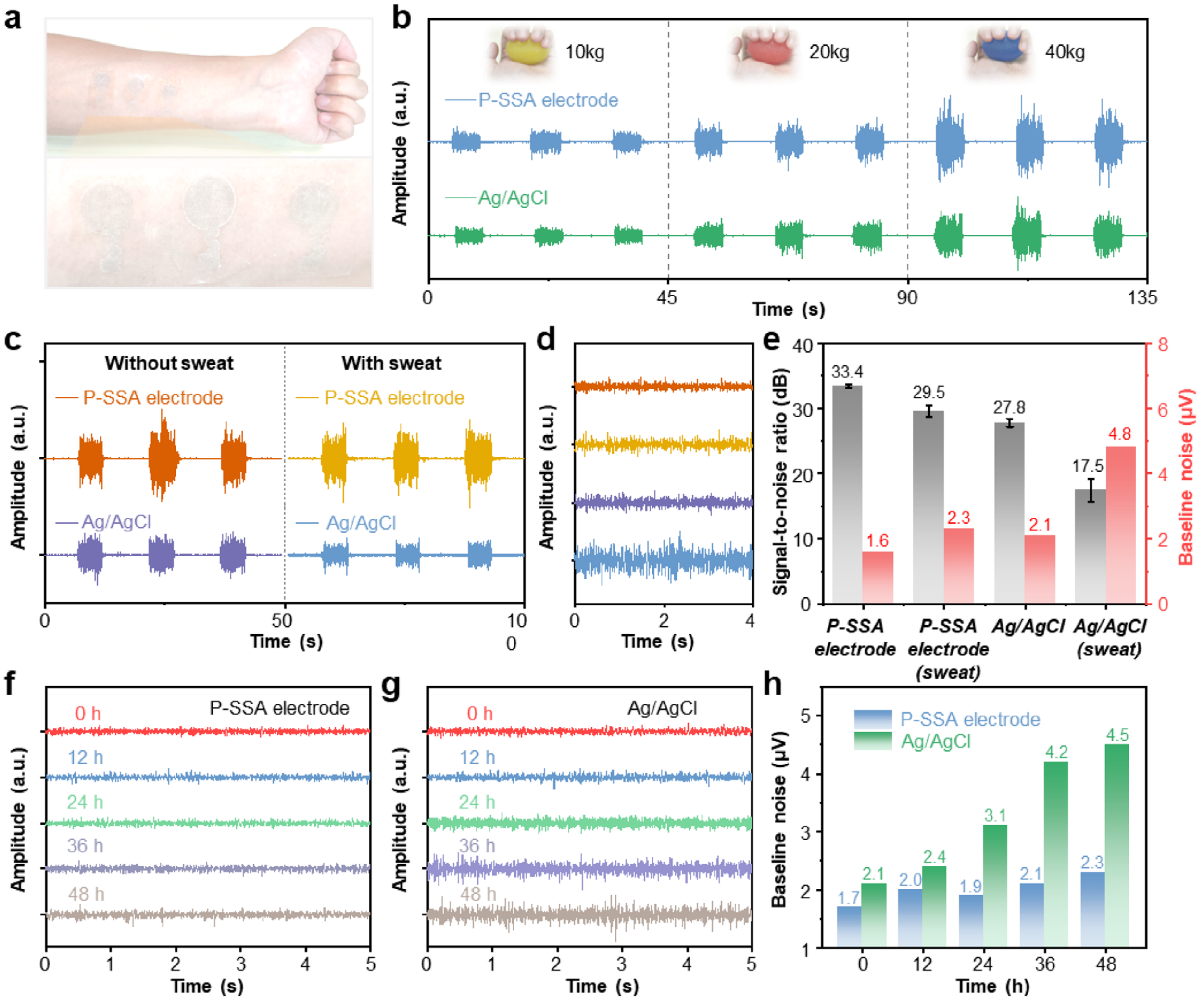

Figure 5. P-SSA electrodes for EMG monitoring. a) Photograph of the P-SSA electrodes attached at wrist flexor muscles for EMG monitoring. b) EMG signals measured by P-SSA electrodes and commercial electrodes when holding elastic balls at different forces. c) EMG signals measured by P-SSA electrodes and commercial gel electrodes without (left) and with (right) sweating and d) magnified view showing the baseline EMG signals. e) Comparison in SNR and root-mean-square (RMS) of baseline noise in EMG signals measured by P-SSA electrodes and commercial gel electrodes under sweating or non-sweating conditions. Comparison in long-term baseline EMG signals between f) SSA electrodes and g) commercial gel electrodes at different times and h) in RMS of the baseline noise.

Supporting Information). Compared to the power during sleeping (Figure S29a, Supporting Information), the EEG during eye opening over cyclic eye closing/opening has a higher signal amplitude (Figure S29b, Supporting Information). Compared with previously reported epidermal EEG and EOG electrodes, the EEG and EOG signals captured by the P-SSA electrodes feature higher power spectral density (PSD) of alpha wave (Table S2, Supporting Information) and larger amplitude in the EOG signals (Table S3, Supporting Information), respectively.

2.6. Epidermal P-SSA Electrode Arrays for Gesture Classification and Recognition

The large-scale patterning and manufacturing of the epidermal P-SSA electrodes can provide an intrinsically stretchable eight-channel epidermal bioelectrode system with eight pairs of electrodes applied to the forearm for gesture recognition (**Figure 6**a,b). After direct connecting the AgNWs network-based terminal pads to the flexible printed circuit board (fPCB) without soldering, the acquired EMG data can be displayed on a custom-built graphical user interface (GUI) in real time (Figure S30, Supporting Information). The EMG signals from eight hand gestures exhibit significant differences (Figure 6c,d), which can be processed by a deep learning algorithm based on a Convolutional Neural Network (CNN) (Figure 6e) for gesture classification and recognition. The CNN model consists of two residual neural network modules with integrated attention mechanisms connected in series, followed by two fully connected layers that output eight classification results. In the gathered 110 groups of data for each gesture, each data segment contains 8 channels with 5500 sampling points in each channel. With 80% of the data randomly

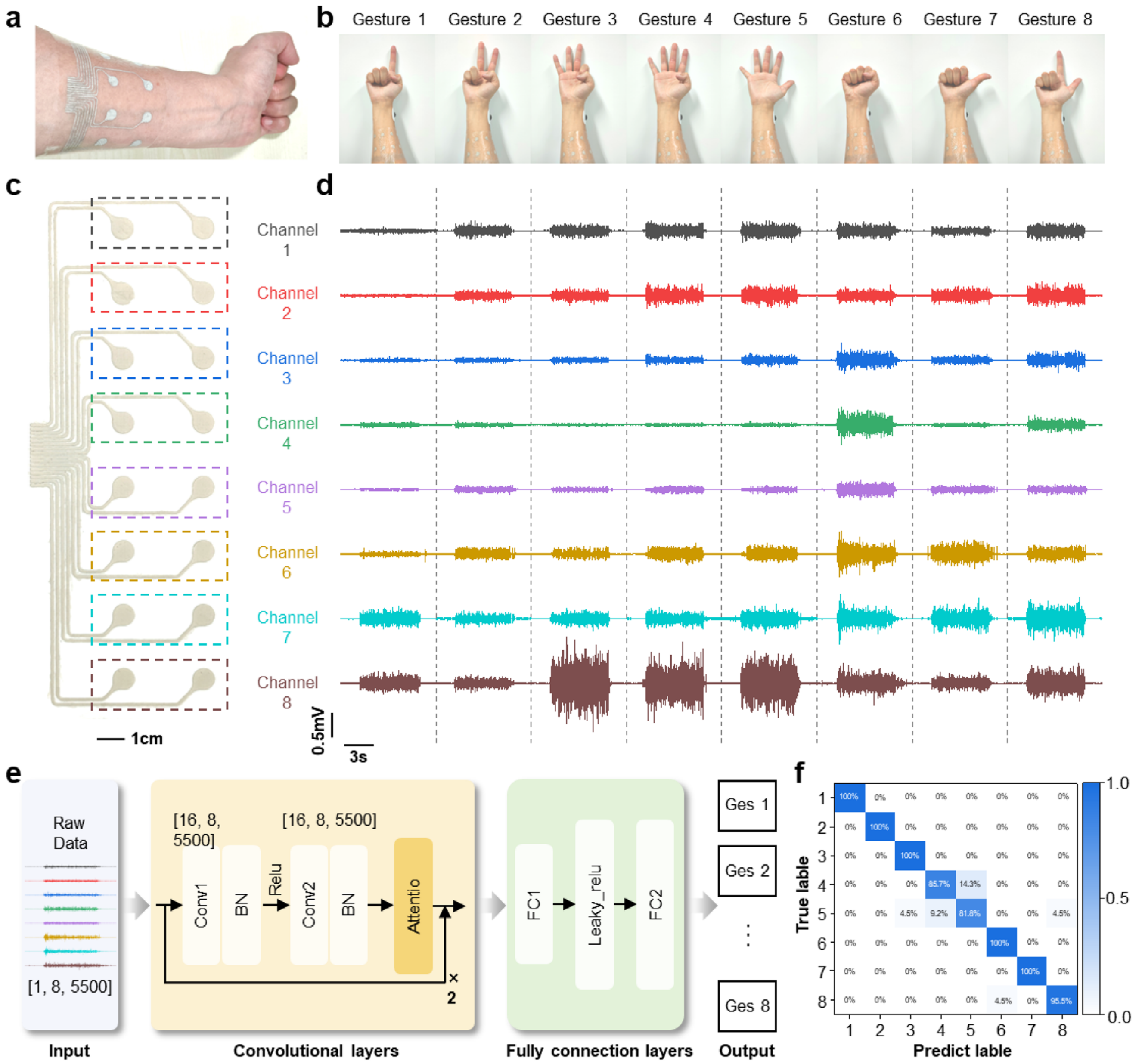

Figure 6. Gesture recognition based on 8-channel EMG signals. a) Photograph of the 8-channel electrode array made from P-SSA electrodes attached to the forearm of a volunteer. b) Photograph of various hand gestures. c) Photograph of the 8-channel electrode array and channel distribution. d) EMG signals recorded by the electrode array when making various gestures. e) Schematic illustration of the deep learning algorithm. f) Confusion matrix of the gesture classification for the 8 gestures.

selected as the training set and the remaining 20% as the test set for each gesture, the CNN model demonstrates a high overall recognition accuracy of 95.4% for the recognition of eight gestures (Figure 6f), showing great potential for applications in human-machine interaction.

3. Conclusion

In summary, the direct patterning and complete transfer of the porous AgNWs network from the LIG onto thin, low-modulus, stretchable perforated substrates result in ultra-conformal and breathable epidermal electrodes. The resulting electrodes intimately conform to the skin with dynamically stable and low contact impedance even over heavy sweating, providing remarkable long-term electrophysiological sensing performances in complex environmental conditions with minimized discomfort and risk of inflammation. The highly efficiency, low-cost, and large-area method also allows facile fabrication of an eight-channel EMG system coupled with a deep learning algorithm for gesture recognition with high accuracy. The results from this study also provide design principles and fabrication methods for future epidermal electronics with long-term stability for high-fidelity health monitoring and high-precision human-robot collaborations.

4. Experimental Section

Materials: Styrene-block-poly (ethylene-ran-butylene)-block-polystyrene (SEBS, Mw-118000) was purchased from Sigma-Aldich. Silbione RT GEL 4317A/B was purchased from Elkem Silicones. The AgNWs dispersion in ethanol (10 mg/mL, average diameter of 90 nm, length of 60 µm) was obtained from XFNANO Corporation. Toluene (99.5%) was purchased from General Reagent. Commercially available polyimide (PI) film was provided by DuPont (Kapton HN, with a thickness of 60 µm). All other materials, solvents, and reagents were obtained from commercial sources and used without further purification.

Preparation of Patterned LIG: The fabrication of patterned LIG started with cleaning of a piece of PI sheet. Subsequently, porous graphene was patterned on PI using a CO_2 infrared laser with a wavelength of 10.6 µm and beam spot size of ≈25 µm (VLS3.50, Universal Laser System, Inc). In all experiments, the setting was fixed at 8% of the maximum power and 11% of the maximum scanning speed. The image density and PPI were set as 6 and 1000. All experiments were performed under ambient conditions.

Preparation of Porous Stretchable Substrates: First, a piece of release paper was attached to a 1 mm-thick glass plate using double-sided tape. After spin-coating (1000 rpm, 30 s) SEBS solution (15 wt.%, in toluene) on the release paper and after evaporating the toluene, Silbione mixed at a 1:1 ratio was spin-coated (1000 rpm, 30 s) and cured on a hot plate at 90 °C for 10 min. Next, CO_2 laser scribing was employed to obtain micro-perforations over the entire substrate, with a perforation diameter of 0.16 mm and spacing of 0.64 mm. The laser scribing was performed using parameters set at 16% power and 15% speed.

Preparation of Ultra-Conformal P-SSA Epidermal Electrodes: The AgNWs dispersion with a precisely controlled amount was first dropped onto the LIG pattern using a pipette. Evaporation of ethanol allowed the AgNWs network to form on the LIG surface with the same patterned shape. Next, the adhesive side of the stretchable substrate on the release paper was applied to the top of AgNWs/LIG. Gent peeling transferred patterned AgNWs to the stretchable substrate to result in the ultra-conformal and breathable epidermal electrodes, which was followed by the removal of the release paper after applying the electrode to the skin.

Characterization: The SEM images were obtained by field emission scanning electron microscopy (Thermo Scientific Apreo 2C). The stress-strain curve was measured by the M230pro (YiGao) at a tensile speed of 30 mm min^{-1}. The 90-degree on-body peeling tests of the epidermal electrodes were also carried out with M230pro (YiGao) by adhering samples with an area of 15 × 60 mm to ethanol-treated human skin at a tensile speed of 30 mm min^{-1}. The sheet resistance was measured using a four-probe sheet resistance meter (HPS58006, Helpass). The skin-contact impedance was measured by using an electrochemical workstation (CHI660E, ChenHua). The water vapor transmission rate was measured based on the ASTM E96 standard. In brief, 10 mL of deionized water was first placed inside a 20 mL glass bottle, which was sealed with a 100 µm thick sample and then placed in a drying cabinet at a temperature of 20 °C and a relative humidity of 25% ± 5%. The mass of the glass bottle was measured every 12 h to calculate the water vapor transmission rate (based on the mass change).

Calculation of Transfer Yield: The AgNWs from the same surface area of LIG before (and after) transfer, represented by manually marked green (and yellow), were first counted to calculate the transfer yield:

$$\text{transfer yield} = \frac{\text{Number of AgNWs} - \text{Number of AgNWs}_{\text{residual}}}{\text{Number of AgNWs}} \tag{1}$$

For the dense AgNWs (5, 10, and 40 µL cm^{-2}) that cannot be counted manually, the number of AgNWs at a concentration of 1 µL/cm^2 on the LIG surface counted from the unit area (10 283.120 ± 3303.771 per mm^2) was scaled with the concentration factor to estimate the number of dense AgNWs before transfer.

Electrophysiological Signal Recording: For all electrophysiological recordings, the epidermal electrodes were conformally attached to human skin, with metal wires connecting the AgNWs layer of the electrodes to a commercialized amplifier (PowerLab 4/26, ADInstruments). ECG signals were recorded with two working electrodes (diameter of 15 mm) placed on the volunteer's inner wrists and the reference electrode placed on the left foot (sampling rate of 1 kHz with a 1–50 Hz bandpass filter). The wireless ECG was recorded by a BLE-based commercial ECG acquisition system (BioBox M2, Sibet CAS) with a 250 Hz sampling rate and 0.1–100 Hz bandpass filter. EMG signals were recorded with three electrodes separated at a distance of 3 cm attached to the forearm (sampling rate of 1 kHz with a bandpass filter of 10–250 Hz and a 50 Hz notch). Gesture recognition used eight pairs of SSA electrodes on the forearm, with a commercial electrode placed under the thumb as a ground electrode. The signal crosstalk and interference were minimized by covering the connection wires with another layer of Silbione for insulation. Vertical EOG signals were measured with two working electrodes placed on the upper and lower eyelids, respectively, and the reference electrode placed on the forehead. Horizontal EOG signals were measured with two working electrodes placed on the outer canthi of each eye and the reference electrode placed on the forehead. The sampling rate of both EOG signals was set to 200 Hz, with a 50 Hz notch. EEG signals were monitored with the test electrode placed on the forehead (Fp1) and the ground/reference electrode placed on the right/left mastoids, according to the international 10/20 system (sampling rate of 200 Hz with a 50 Hz notch). The signal-to-noise ratio (SNR) of the electrophysiological signals was calculated as: $\text{SNR(dB)} = 20\log 10(A_{\text{signal}}/A_{\text{noise}})$, where A_{signal} and A_{noise} represented the root-mean-square of signal and noise, respectively.

Experiments Involving Human Participants: The human subject study was approved by the Medical Ethics Committee of The People's Hospital of Suzhou New District (Approval No. 2023–141). All human subjects gave written and informed consent before participation in the studies.

Supporting Information

Supporting Information is available from the Wiley Online Library or from the author.

Acknowledgement

J.L. and S.Z. contributed equally to this work. S.Z. acknowledges the support provided by the National Natural Science Foundation of China (Grant No. 62301556), the Shandong Natural Science Foundation (ZR2023QH203), excellent postdoctoral fellows of Jiangsu province, and also would like to acknowledge Qi Lu's love and parents' support. H.C. acknowledges the support provided by NIH (Award No. R21EB030140), NSF (Grant Nos. 2309323 and 2319139), and Penn State University.

Conflict of Interest

The authors declare no conflict of interest.

Data Availability Statement

The data that support the findings of this study are available from the corresponding author upon reasonable request.

Keywords

assisted transfer and patterning, electrophysiological monitoring, epidermal electrodes, ultra-conformal and long-term stable

Received: February 19, 2025
Published online:

[1] a) C. F. Wang, C. H. Wang, Z. L. Huang, S. Xu, *Adv. Mater.* **2018**, *30*, 1801368; b) Y. Y. Zhang, T. Y. Zhang, Z. D. Huang, J. Yang, *Adv. Sci.* **2022**, *9*, 2105084; c) S. Q. Guo, K. J. Wu, C. P. Li, H. Wang, Z. Sun, D. W. Xi, S. Zhang, W. P. Ding, M. E. Zaghloul, C. N. Wang, F. A. Castro, D. Yang, Y. L. Zhao, *Matter* **2021**, *4*, 969; d) B. Zhang, J. Lei, D. P. Qi, Z. Y. Liu, Y. Wang, G. W. Xiao, J. S. Wu, W. N. Zhang, F. W. Huo, X. D. Chen, *Adv. Funct. Mater.* **2018**, *28*, 1801683; e) C. J. Wan, G. Chen, Y. M. Fu, M. Wang, N. Matsuhisa, S. W. Pan, L. Pan, H. Yang, Q. Wan, L. Q. Zhu, X. D. Chen, *Adv. Mater.* **2018**, *30*, 1801291; f) C. J. Wan, P. Q. Cai, M. Wang, Y. Qian, W. Huang, X. D. Chen, *Adv. Mater.* **2020**, *32*, 1902434.

[2] a) L. Tian, B. Zimmerman, A. Akhtar, K. J. Yu, M. Moore, J. Wu, R. J. Larsen, J. W. Lee, J. Li, Y. Liu, B. Metzger, S. Qu, X. Guo, K. E. Mathewson, J. A. Fan, J. Cornman, M. Fatina, Z. Xie, Y. Ma, J. Zhang, Y. Zhang, F. Dolcos, M. Fabiani, G. Gratton, T. Bretl, L. J. Hargrove, P. V. Braun, Y. Huang, J. A. Rogers, *Nat. Biomed. Eng.* **2019**, *3*, 194; b) J. Cheng, J. Shang, S. Yang, J. Dou, X. Shi, X. Jiang, *Adv. Funct. Mater.* **2022**, *32*, 2200444; c) S. Park, S. Ban, N. Zavanelli, A. E. Bunn, S. Kwon, H.-r. Lim, W.-H. Yeo, J.-H. Kim, *ACS Appl. Mater. Interfaces* **2023**, *15*, 2092.

[3] R. Xie, Q. Li, L. Teng, Z. Cao, F. Han, Q. Tian, J. Sun, Y. Zhao, M. Yu, D. Qi, P. Guo, G. Li, F. Huo, Z. Liu, *npj Flexible Electron.* **2022**, *6*, 75.

[4] J. Parvizi, S. Kastner, *Nat. Neurosci.* **2018**, *21*, 474.

[5] T. Kusayama, J. Wong, X. Liu, W. He, A. Doytchinova, E. A. Robinson, D. E. Adams, L. S. Chen, S.-F. Lin, K. Davoren, R. G. Victor, C. Cai, M.-Y. Dai, Y. Tian, P. Zhang, D. Ernst, R. H. Rho, M. Chen, Y.-M. Cha, D. R. Walega, T. H. Everett, P.-S. Chen, *Nat. Protoc.* **2020**, *15*, 1853.

[6] M. Roudjane, S. Tam, Q. Mascret, C. L. Fall, M. Bielmann, R. A. D. d. Faria, L. J. Bouyer, B. Gosselin, Y. Messaddeq, *IEEE Sens. J.* **2019**, *19*, 11624.

[7] Y. Liu, B. Xu, Z. Xie, J. Yang, Y. Liu, Y. Yang, H. Xu, *ACS Appl. Mater. Interfaces* **2023**, *15*, 59787.

[8] a) E. Huigen, A. Peper, C. A. Grimbergen, *Med. Biol. Eng. Comput.* **2002**, *40*, 332; b) P. Leleux, C. Johnson, X. Strakosas, J. Rivnay, T. Hervé, R. M. Owens, G. G. Malliaras, *Adv. Healthcare Mater.* **2014**, *3*, 1377.

[9] A. Aguzin, A. Dominguez-Alfaro, M. Criado-Gonzalez, S. Velasco-Bosom, M. L. Picchio, N. Casado, E. Mitoudi-Vagourdi, R. J. Minari, G. G. Malliaras, D. Mecerreyes, *Mater. Horiz.* **2023**, *10*, 2516.

[10] S. Liu, Y. Rao, H. Jang, P. Tan, N. Lu, *Matter* **2022**, *5*, 1104.

[11] S. Luebberding, N. Krueger, M. Kerscher, *Int. J. Cosmetic Sci.* **2013**, *35*, 477.

[12] X. Zou, J. Xue, X. Li, C. P. Y. Chan, Z. Li, P. Li, Z. Yang, K. W. C. Lai, *ACS Appl. Mater. Interfaces* **2023**, *15*, 19374.

[13] Y. Li, A. Veronica, J. Ma, H. Y. Y. Nyein, *Adv. Mater.* **2024**, *n/a*, 2408456.

[14] Y. Lin, Q. Li, C. Ding, J. Wang, W. Yuan, Z. Liu, W. Su, Z. Cui, *Nano Res.* **2022**, *15*, 4590.

[15] H.-R. Lim, H. S. Kim, R. Qazi, Y.-T. Kwon, J.-W. Jeong, W.-H. Yeo, *Adv. Mater.* **2020**, *32*, 1901924.

[16] Y. Wang, H. Haick, S. Y. Guo, C. Y. Wang, S. Lee, T. Yokota, T. Someya, *Chem. Soc. Rev.* **2022**, *51*, 3759.

[17] Y. Luo, M. R. Abidian, J.-H. Ahn, D. Akinwande, A. M. Andrews, M. Antonietti, Z. Bao, M. Berggren, C. A. Berkey, C. J. Bettinger, J. Chen, P. Chen, W. Cheng, X. Cheng, S.-J. Choi, A. Chortos, C. Dagdeviren, R. H. Dauskardt, C.-a. Di, M. D. Dickey, X. Duan, A. Facchetti, Z. Fan, Y. Fang, J. Feng, X. Feng, H. Gao, W. Gao, X. Gong, C. F. Guo, et al., *ACS Nano* **2023**, *17*, 6.

[18] Y. Gu, Z. Qiu, S. Zhu, H. Lu, L. Peng, G. Zhang, Z. Wu, X. Gui, Z. Qin, B.-r. Yang, *Nano Res.* **2023**, *16*, 11303.

[19] a) W. Zhou, S. Yao, H. Wang, Q. Du, Y. Ma, Y. Zhu, *ACS Nano* **2020**, *14*, 5798; b) J.-H. Kim, S.-R. Kim, H.-J. Kil, Y.-C. Kim, J.-W. Park, *Nano Lett.* **2018**, *18*, 4531.

[20] a) L. Zhang, K. S. Kumar, H. He, C. J. Cai, X. He, H. Gao, S. Yue, C. Li, R. C.-S. Seet, H. Ren, J. Ouyang, *Nat. Commun.* **2020**, *11*, 4683; b) H. Wu, G. G. Yang, K. H. Zhu, S. Y. Liu, W. Guo, Z. Jiang, Z. Li, *Adv. Sci.* **2021**, *8*, 2001938; c) T. Cui, Y. Qiao, D. Li, X. Huang, L. Yang, A. Yan, Z. Chen, J. Xu, X. Tan, J. Jian, Z. Li, S. Ji, H. Liu, Y. Yang, X. Zhang, T.-L. Ren, *Chem. Eng. J.* **2023**, *455*, 140690.

[21] H. Wu, D. Kong, Z. Ruan, P.-C. Hsu, S. Wang, Z. Yu, T. J. Carney, L. Hu, S. Fan, Y. Cui, *Nat. Nanotechnol.* **2013**, *8*, 421.

[22] G. Liu, Z. Tian, Z. Yang, Z. Xue, M. Zhang, X. Hu, Y. Wang, Y. Yang, P. K. Chu, Y. Mei, L. Liao, W. Hu, Z. Di, *Nat. Electron.* **2022**, *5*, 275.

[23] G. Ye, Z. Song, T. Yu, Q. Tan, Y. Zhang, T. Chen, C. He, L. Jin, N. Liu, *ACS Appl. Mater. Interfaces* **2020**, *12*, 1486.

[24] Y. Fang, Y. Li, X. Wang, Z. Zhou, K. Zhang, J. Zhou, B. Hu, *Small* **2020**, *16*, 2000450.

[25] J. Huang, L. Wang, Y. M. Jin, P. Lu, L. L. Wang, N. N. Bai, G. Li, P. Zhu, Y. Wang, J. M. Zhang, Z. G. Wu, C. F. Guo, *Adv. Funct. Mater.* **2020**, *30*, 2001518.

[26] K. Yang, S. Zhang, Y. Yang, X. Liu, J. Li, B. Bao, C. Liu, H. Yang, K. Guo, H. Cheng, *Mater. Des.* **2024**, *243*, 113029.

[27] Y. Zheng, Y. Li, Y. Zhao, X. Lin, S. Luo, Y. Wang, L. Li, C. Teng, X. Wang, G. Xue, D. Zhou, *Nano Energy* **2023**, *107*, 108092.

[28] a) D. Yoo, D.-J. Won, W. Cho, S. Kim, J. Kim, *Small Methods* **2021**, *5*, 2101049; b) Q. Huang, Y. Zhu, *ACS Appl. Mater. Interfaces* **2021**, *13*, 60736.

[29] a) T. Pinheiro, R. Correia, M. Morais, J. Coelho, E. Fortunato, M. G. F. Sales, A. C. Marques, R. Martins, *ACS Nano* **2022**, *16*, 20633; b) J. Lin, Z. Peng, Y. Liu, F. Ruiz-Zepeda, R. Ye, E. L. G. Samuel, M. J. Yacaman, B. I. Yakobson, J. M. Tour, *Nat. Commun.* **2014**, *5*, 5714.

[30] a) S. Deshmukh, K. Ghosh, M. Pykal, M. Otyepka, M. Pumera, *ACS Nano* **2023**, *17*, 20; b) S. Deshmukh, D. Banerjee, J. S. Marin Quintero, S. J. Fishlock, J. McLaughlin, P. R. Waghmare, S. S. Roy, *Carbon* **2021**, *182*, 605.

[31] a) L. X. Duy, Z. W. Peng, Y. L. Li, J. B. Zhang, Y. S. Ji, J. M. Tour, *Carbon* **2018**, *126*, 472; b) H. Wang, Z. Zhao, P. Liu, X. Guo, *Biosensors* **2022**, *12*, 55.

[32] a) Q. Gao, F. Sun, Y. Li, L. Li, M. Liu, S. Wang, Y. Wang, T. Li, L. Liu, S. Feng, X. Wang, S. Agarwal, T. Zhang, *Nano-Micro Lett.* **2023**, *15*, 139; b) J. Xu, X. Li, H. Chang, B. Zhao, X. Tan, Y. Yang, H. Tian, S. Zhang, T.-L. Ren, *ACS Nano* **2022**, *16*, 6687; c) Z. Zhang, J. Yang, H. Wang, C. Wang, Y. Gu, Y. Xu, S. Lee, T. Yokota, H. Haick, T. Someya, Y. Wang, *Sci. Adv.* **2024**, *10*, eadj5389.

[33] E. T. McAdams, J. Jossinet, A. Lackermeier, F. Risacher, *Med. Biol. Eng. Comput.* **1996**, *34*, 397.

[34] Y. Liu, Y. Cheng, L. Shi, R. Wang, J. Sun, *ACS Appl. Mater. Interfaces* **2022**, *14*, 12812.

[35] Q. Li, G. Chen, Y. Cui, S. Ji, Z. Liu, C. Wan, Y. Liu, Y. Lu, C. Wang, N. Zhang, Y. Cheng, K.-Q. Zhang, X. Chen, *ACS Nano* **2021**, *15*, 9955.

[36] M. A. Zahed, M. Sharifuzzaman, H. Yoon, M. Asaduzzaman, D. K. Kim, S. Jeong, G. B. Pradhan, Y. D. Shin, S. H. Yoon, S. Sharma, S. Zhang, J. Y. Park, *Adv. Funct. Mater.* **2022**, *32*, 2208344.

[37] H.-L. Peng, Y.-l. Sun, C. Bi, Q.-F. Li, *Measurement* **2022**, *190*, 110782.

[38] Y. Liu, C. Wang, J. Xue, G. Huang, S. Zheng, K. Zhao, J. Huang, Y. Wang, Y. Zhang, T. Yin, Z. Li, *Adv. Healthcare Mater.* **2022**, *11*, 2200653.